

# PROMPT AS KNOWLEDGE BANK: BOOST VISION-LANGUAGE MODEL VIA STRUCTURAL REPRESENTATION FOR ZERO-SHOT MEDICAL DETECTION

**Anonymous authors**

Paper under double-blind review

## ABSTRACT

Zero-shot medical detection enhances existing models without relying on annotated medical images, offering significant clinical value. By using grounded vision-language models (GLIP) with detailed disease descriptions as prompts, doctors can flexibly incorporate new disease characteristics to improve detection performance. However, current methods often oversimplify prompts as mere equivalents to disease names and lacks the ability to incorporate visual cues, leading to coarse image-description alignment. To address this, we propose StructuralGLIP, a framework that encodes prompts into a latent knowledge bank, enabling more context-aware and fine-grained alignment. By selecting and matching the most relevant features from image representations and the knowledge bank at layers, StructuralGLIP captures nuanced relationships between image patches and target descriptions. This approach also supports category-level prompts, which can remain fixed across all instances of the same category and provide more comprehensive information compared to instance-level prompts. Extensive experiments show that StructuralGLIP outperforms previous methods across eight zero-shot medical detection benchmarks. Additionally, it can be seamlessly integrated into GLIP models fine-tuned on medical data, further enhancing performance with additional linguistic prompts and showcasing its practical value alongside supervised models. The code will be available after the review.

## 1 INTRODUCTION

Zero-shot medical detection is crucial in healthcare as it enhances detection capabilities without requiring additional annotated medical images, even after model fine-tuning (Badawi et al., 2024; Mahapatra et al., 2021; Qin et al., 2022). This is particularly valuable in clinical settings, where doctors often encounter new disease characteristics not previously documented. In such cases, clinicians can temporarily create custom prompts to guide the detection process, allowing models to adapt to novel scenarios more effectively. Recent studies have explored the potential of grounded language-image pre-training models (GLIP) (Phan et al., 2024; Tiu et al., 2022; Li et al., 2022c; Yao et al., 2022) to reduce dependence on annotations by leveraging prior knowledge. These models conduct detection by contrasting image features with descriptive texts, known as *contextual prompts*, generated by visual question-answer models for query objects. To adapt GLIP to the medical domain, recent works (Qin et al., 2022; Wu et al., 2023b; Guo et al., 2023) have employed medically enhanced question-answer models like PubMedBERT (Gu et al., 2021) and BLIP (Li et al., 2022a) to create attribute-rich prompts. These prompts capture nuanced characteristics of query targets, improving domain adaptation and performance beyond traditional supervised training.

However, existing contextual prompt-based methods often suffer from coarse alignment between images and target descriptions, resulting in two key issues. First, these methods typically treat prompts as contexts that are equivalent to the target, easily causing distribution shift problems to the target’s representation. This often leads to sub-optimal detection performance and misalignment with the actual visual cues in the image (see Fig. E). Second, these methods struggle to handle category-level descriptions, such as "tissue with pink or red color, irregular or round shape" for a "bump". This is because the context-based prompt methods can not precisely match the most relevant

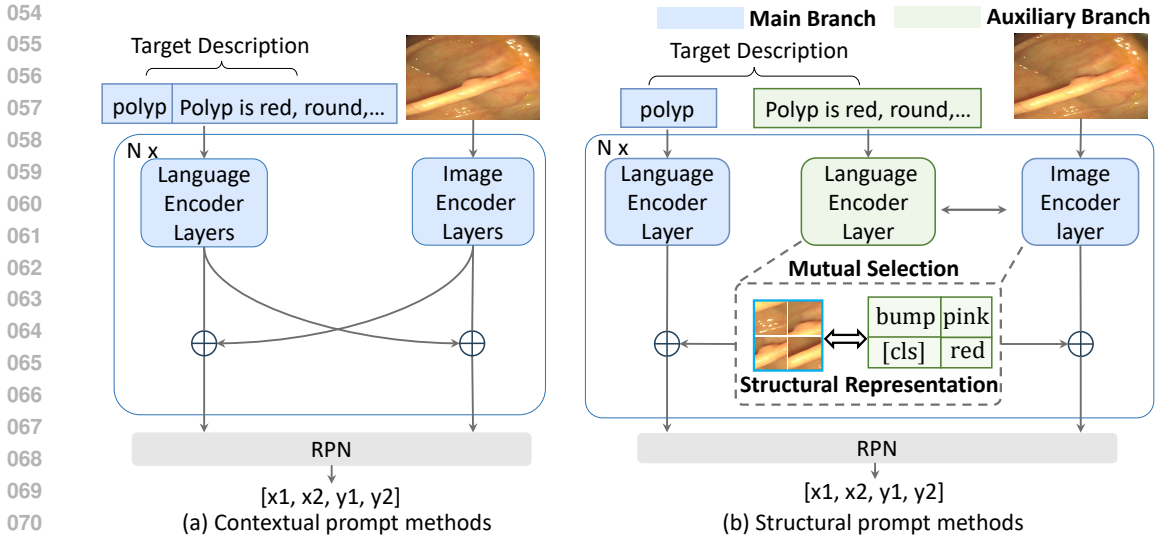


Figure 1: (a) Contextual prompt methods directly concatenate the prompt and target. (b) Our structural prompt method encodes prompts into a latent knowledge bank.

prompt with the input image, causing misalignment in detecting nuanced variations within medical images.

To address the aforementioned issues, we present StructuralGLIP, a novel zero-shot medical detection model that derives *structural representations*, which are delicately organized sets of features specifically designed to represent the nuances of the target and the input image. Specifically, as shown in Fig. 1, instead of simply concatenating prompts with the target, StructuralGLIP adopts a dual-branch architecture. The main branch processes the target name and input image, while the auxiliary branch encodes the prompts into a latent knowledge bank. At each layer, rather than directly performing cross-modal fusion between vision and language features, StructuralGLIP introduces a mutual selection mechanism. This mechanism matches vision features from the main branch with relevant prompt features stored in the latent knowledge bank, where we extract latent prompt tokens and latent vision tokens that both highly relevant to the target and the current input image, forming fine-grained structural representations. Once these structural representations are formed, the image and language features from the main branch are fused with the selected prompt tokens via cross-modality multi-head attention (Vaswani et al., 2017). This enhances the overall feature alignment and improves the fusion process within the main branch. Conceptually, the hierarchical knowledge bank in StructuralGLIP functions like a memory system (Bi, 2021; Paivio, 2013). As the image is processed, relevant knowledge is dynamically retrieved from the bank. This enables the model to better align the image features with the prompt information, resulting in more accurate and context-aware detection.

In this way, StructuralGLIP can address the challenge of effectively utilizing category-level prompts, which provide broader yet consistent information for all instances within the same category (see Fig. B for visualization). StructuralGLIP’s instance-wise selection mechanism ensures that even fixed category-level prompts are dynamically aligned with the specific visual features of each instance. This not only improves detection precision but also enhances efficiency, as category-level prompts can remain fixed across instances of the same category. To validate the proposed method, we benchmark StructuralGLIP against previous state-of-the-art methods on eight datasets under endoscopy, microscopy, photography, and radiology four imaging conditions, and conduct a comprehensive analysis towards StructuralGLIP’s structural representations. The primary contributions of our work are as follows:

- We introduce StructuralGLIP, a novel architecture that achieves adaptive, context-aware alignment between visual features and target descriptions by utilizing a dual-branch structure with mutual selection, enhancing the precision of medical object detection.
- We propose the use of category-level prompts, which remain fixed for all instances of the same target. Unlike instance-level prompts, category-level prompts provide more comprehensive prior

108 knowledge about the target disease, reducing the need for prompt generation for each individual  
109 image while maintaining strong detection performance.

- 110 • We explore zero-shot medical detection in more practical settings by demonstrating how zero-  
111 shot enhancement can further improve the performance of models fine-tuned on medical data.  
112 StructuralGLIP not only surpasses fully supervised methods such as RetinaNet but also seamlessly  
113 integrates into GLIP models fine-tuned on medical datasets, achieving an average improvement of  
114 +4% AP.

## 115 116 2 RELATED WORK

117  
118 **Zero-shot medical detection** aims to identify and locate pathology concepts in medical images  
119 without relying on annotated data from the target domain (Vilouras et al., 2024; Qin et al., 2022;  
120 Paul et al., 2021; Mahapatra et al., 2021; Sahasrabudhe et al., 2020; Le Bescond et al., 2022).  
121 Classical strategies include cross-domain generalization (Bian et al., 2022; Bansal et al., 2024) and  
122 unsupervised learning (Sahasrabudhe et al., 2020; Le Bescond et al., 2022; Paul et al., 2021). Cross-  
123 domain generalization utilizes data from related domains under varied conditions, such as different  
124 imaging techniques (Bian et al., 2022) or demographic differences (Bansal et al., 2024), to adapt  
125 models across diverse scenarios. Unsupervised learning methods leverage side information to bypass  
126 direct supervision, such as using cell nuclei structure for image resolution analysis (Sahasrabudhe  
127 et al., 2020), employing GANs with public annotations to enhance mask quality (Le Bescond et al.,  
128 2022), and correlating medical reports with disease features to increase detection accuracy (Paul  
129 et al., 2021). However, these methods are often tightly coupled to specific data priors and exhibit a  
130 considerable performance gap compared to supervised models, limiting their clinical significance.

131 Recent approaches have integrated expert-level knowledge into vision-language models trained on  
132 natural images to facilitate domain transfer (Liu et al., 2023a; Lai et al., 2024; Tiu et al., 2022; Wu  
133 et al., 2023a; Zhang et al., 2023). However, most of these efforts focus on medical classification, while  
134 the more practical and complex task of medical detection remains underexplored. For example, (Qin  
135 et al., 2022) conducted a comprehensive study on medical detection using prompts generated by  
136 a medically-enhanced language model, PubMedBERT (Gu et al., 2021). Follow-up studies (Wu  
137 et al., 2023b; Lu et al., 2023; Phan et al., 2024) employed BLIP (Li et al., 2022a) to generate  
138 image-specific linguistic attributes, or used GPT (Achiam et al., 2023) to detail target concepts with  
139 nuanced descriptions. Recent work (Guo et al., 2023) further advanced this approach by introducing  
140 an ensemble strategy for fusing multiple prompts to improve detection accuracy. However, these  
141 methods require unique prompts for each instance, significantly reducing efficiency. Our method,  
142 StructuralGLIP, addresses these challenges by introducing a vision-language model that leverages a  
143 knowledge bank to store a wide range of prompts, enabling instance-dynamic prompt selection in the  
144 latent feature space.

145 **Knowledge-bank-based prompt method** is initially developed for continual learning, which utilizes  
146 a prompt pool designed to enhance cross-domain generalization (Wang et al., 2022b;a; Smith et al.,  
147 2023; Wang et al., 2023; Du et al., 2022). Previous works (Wang et al., 2022b;a) select top- $k$  prompts  
148 aligned with input image features, facilitating domain-specific modeling. Recent advances have  
149 evolved this strategy, replacing the top- $k$  prompt selection with a more flexible continuous prompt  
150 fusion strategy (Smith et al., 2023), exploring its potential for vision-language model (Wang et al.,  
151 2023), and expanding applications to open-vocabulary detection tasks (Du et al., 2022). However,  
152 these methods typically require an additional training phase and are restricted to prompt retrieval in  
153 the input layer. In contrast, StructuralGLIP explores a linguistically accessible avenue by directly  
154 utilizing the attributes predefined by the generative models and embeds these attribute prompts into  
155 a hierarchy knowledge bank situated within an auxiliary branch to achieve a layer-wise selection  
156 process.

## 157 3 METHODOLOGY

### 158 3.1 PRELIMINARIES

159 **Zero-shot medical object detection** means improving the model’s medical detection performance  
160 without the use of supervised image labels. This formulation emphasizes "further improvement  
161

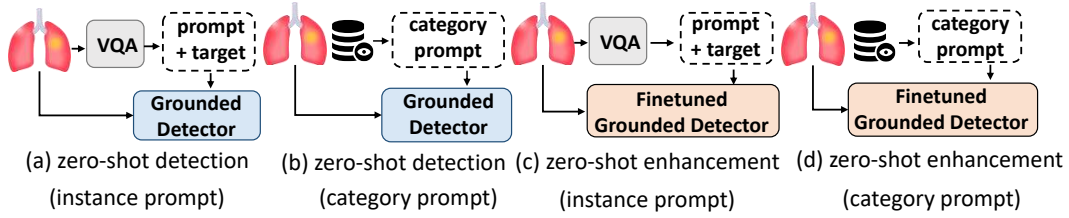


Figure 2: Experimental settings for zero-shot medical detection and enhancement.

without supervised images", which contains two experimental settings. Firstly, in the classical setting, the model, without fine-tuning on medical datasets, uses pre-trained vision-language concepts with prompts to infer medical concepts (see Fig. 2 (a) and (b)). Secondly, considering the clinical setting prefers supervised models for their excellent performance, we propose a zero-shot enhancement setting. This involves fine-tuning the model on medical datasets first, and then using prompts to further improve performance on unseen medical images, without requiring additional labels (see Fig. 2(c) and (d)). This setting mirrors real-world clinical needs, where models can be continuously improved with new knowledge without the need for labeled data.

**GLIP** redefines object detection as a phrase-grounding task by employing a late fusion dual-tower architecture to align image and text features. It uses separate backbones  $Enc_I$  and  $Enc_T$  to extract initial encodings  $O^0$  and  $P^0$  for images and text, respectively. These features are then integrated through a cross-modal multi-head attention module (X-MHA), enabling fine-grained interaction between the modalities. The integration of image and text features through the deep fusion module (X-MHA) is formalized as follows:

$$O_{t2v}^i, P_{v2t}^i = \text{X-MHA}(O^i, P^i), \quad (1)$$

$$O^{i+1} = f_I^i(O^i + O_{t2v}^i), \quad P^{i+1} = f_L^i(P^i + P_{v2t}^i), \quad (2)$$

where  $f_I^i$  and  $f_L^i$  are the  $i^{\text{th}}$  encoder layers for images and text, respectively, and  $i \in [1, N]$ . After  $N$  layers of interaction, the final image and text representations are denoted as  $O^N$  and  $P^N$ , respectively. These representations are used as input to the RPN for generating object proposals:

$$R_{\text{GLIP}} = \text{RPN}(O^N, P^N), \quad (3)$$

where  $R_{\text{GLIP}}$  denotes the set of region proposals of GLIP generated by the RPN. Each proposal  $r \in R$  is characterized by its bounding box coordinates and a confidence score, indicating the likelihood of the region containing the target object.

### 3.2 ZERO-SHOT DUAL-BRANCH PROMPT FRAMEWORK

In the proposed StructuralGLIP framework, we introduce a novel zero-shot architecture to achieve fine-grained alignment between target description and medical images. The overall pipeline is shown in Fig. 3.

**Structurally separated auxiliary and main branches.** StructuralGLIP adopts a dual-branch architecture. The main branch processes the target name and input image, while the auxiliary branch encodes the prompts into a latent knowledge bank. Given the object target  $T$  and the prompt  $Prompt$ , the initial representations  $T^0$  and  $B^0$  are obtained as follows:

$$T^0 = \text{Enc}_{L_1}(T), \quad B^0 = \text{Enc}_{L_2}(Prompt), \quad (4)$$

where  $\text{Enc}_{L_1}$  and  $\text{Enc}_{L_2}$  are language backbones with shared parameters for the main and auxiliary branches, respectively. Here,  $T^0$  and  $B^0 \in \mathbb{R}^{N_l \times D}$  represent the initial encoded features of the target and prompts, with [PAD] tokens used to pad the input sentences to a uniform length  $N_l$ . The encoded prompts  $B^0$  are then processed through the language encoder layers:

$$B^i = f_{L_2}^i(B^{i-1}), \quad (5)$$

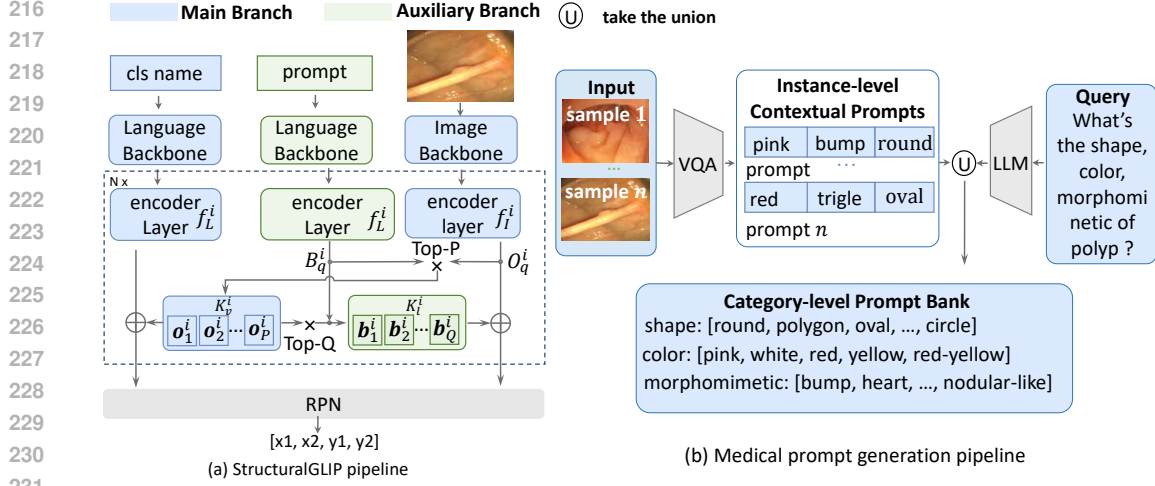


Figure 3: Pipeline of the proposed method and the automatic prompt generation.

where  $f_{L_2}^i$  is the  $i^{\text{th}}$  language encoder layer of the auxiliary branch, and  $B^i$  denotes representation of prompt bank at the  $i^{\text{th}}$  layer.

### Mutual prompt selection mechanism for structural representation in the auxiliary branch.

This mechanism identifies mutually relevant tokens between the visual tokens from the main branch and the linguistic tokens from the auxiliary branch. For selecting the Top- $P$  relevant visual tokens from the latent representation of the input image, we calculate their similarity with latent prompt features. The visual and linguistic representations in the  $i$ -th layer are denoted as  $O_q^i \in \mathbb{R}^{N_v \times D}$  and  $B_q^i \in \mathbb{R}^{N_l \times D}$ , respectively. We have the following:

$$O_q^i = [\mathbf{o}_1^i, \mathbf{o}_2^i, \dots, \mathbf{o}_{N_v}^i], \quad \mathcal{K}_v^i = \text{Top-}P^{\max} \left( [\text{key} = \mathbf{o}_j^i, \text{value} = \mathbf{o}_j^i \mathbf{B}_q^i]_{j=1}^{N_v} \right), \quad (6)$$

where  $\text{Top-}P^{\max}([\text{key}, \text{value}])$  denotes selecting the keys with the Top- $P$  maximal values,  $\mathcal{K}_v^i$  is the selected visual tokens in the  $i$ -th encoder layer, and  $N_v$  is the token length of the visual encoder. Similarly, to select the Top- $Q$  tokens from the latent representation of the prompt, we use the similarity to the selected visual tokens  $\mathcal{K}_v^i$ :

$$B_q^i = [\mathbf{b}_1^i, \mathbf{b}_2^i, \dots, \mathbf{b}_{N_l}^i], \quad \mathcal{K}_l^i = \text{Top-}Q^{\max} \left( [\text{key} = \mathbf{b}_j^i, \text{value} = \mathbf{b}_j^i \mathcal{K}_v^i]_{j=1}^{N_l} \right), \quad (7)$$

where  $\text{Top-}Q^{\max}([\text{key}, \text{value}])$  denotes selecting the keys with the Top- $Q$  maximal values.  $\mathcal{K}_l^i$  is the selected linguistic tokens in the  $i$ -th layer, and  $N_l$  is the token length of the language encoder. These selected prompt tokens  $\mathcal{K}_v^i$  and  $\mathcal{K}_l^i$  are highly relevant to the target and the current input image, forming fine-grained structural representations.

**Deep fusion with the vision-language prompt in the main branch.** Once the structural representations are obtained, we serve these selected prompt tokens  $\mathcal{K}_v^i$  and  $\mathcal{K}_l^i$  as latent prompts for the deep fusion process of GLIP. Instead of using the auxiliary language encoder to enhance the features, the main branch's vision and language encoders leverage the knowledge from the selected tokens  $\mathcal{K}_l^i$  and  $\mathcal{K}_v^i$ . This ensures that comprehensive knowledge from the prompts can be extracted precisely and applied in an instance-wise manner to enhance the detection process. Specifically, we employ a multi-head attention (MHA) mechanism Vaswani et al. (2017) for  $(\mathcal{K}_v^i, T_q^i)$  and  $(\mathcal{K}_l^i, O_q^i)$ :

$$O_{t2v}^{\text{top}Q} = \text{MHA}(\text{Q} = \mathcal{K}_v^i, \text{KV} = T_q^i) \quad T_{v2t}^{\text{top}P} = \text{MHA}(\text{Q} = \mathcal{K}_l^i, \text{KV} = O_q^i), \quad (8)$$

where Q denotes the query item and KV denotes the key and value items for MHA, and  $O_{t2v}^{\text{top}Q}$ ,  $T_{v2t}^{\text{top}P}$  is the input image and target representations that incorporate the prior knowledge about the target from the selected tokens, respectively. These representations are then combined with the original layer representation using the following residual connection:

270  
271  
272  
273  
274  
275  
276  
277  
278  
279  
280  
281  
282  
283  
284  
285  
286  
287  
288  
289  
290  
291  
292  
293  
294  
295  
296  
297  
298  
299  
300  
301  
302  
303  
304  
305  
306  
307  
308  
309  
310  
311  
312  
313  
314  
315  
316  
317  
318  
319  
320  
321  
322  
323

$$O^{i+1} = f_I^i(O^i + O_{t2v}^{\text{top}Q}), \quad T^{i+1} = f_L^i(T^i + T_{v2t}^{\text{top}P}). \quad (9)$$

This deep fusion mechanism ensures that the model dynamically integrates relevant prompts at each layer, significantly enhancing instance-specific adaptation for zero-shot medical detection. After  $N$  layers of interaction, we obtain the final image and text representations from the main branch, denoted as  $O^N$  and  $T^N$ , respectively. Here,  $T^N$  represents the target’s representation, which has fused prompt information relevant to the current instance, achieving a more precise alignment with  $O^N$ . These representations are then used as input to the RPN for generating object proposals:

$$R_{\text{StructuralGLIP}} = \text{RPN}(O^N, T^N), \quad (10)$$

where  $R_{\text{StructuralGLIP}}$  denotes the set of region proposals generated by the RPN in StructuralGLIP. This process effectively combines the structural representations from both the visual and language modalities to achieve accurate and context-aware zero-shot detection.

### 3.3 INSTANCE/CATEGORY-LEVEL MEDICAL PROMPT AUTOMATIC GENERATION

As shown in Fig. 3(b), we propose a dual-level prompt generation mechanism that constructs a comprehensive prompt repository at both the instance and category levels. This enables StructuralGLIP to dynamically apply the most relevant knowledge during inference, significantly improving detection accuracy.

**Instance-level Prompt Generation.** For each medical image, we generate instance-specific prompts to capture unique visual features such as shape, color, and morphology using a Visual Question Answering (VQA) model like BLIP Li et al. (2022a). We query the model with targeted questions (e.g., “What is the shape of the polyp?”), and the responses form a set of instance-level contextual prompts (e.g., “[pink-white, bump-like, round]”). This process ensures that the model can dynamically adapt to the specific characteristics of each image, providing fine-grained descriptions that are crucial for precise detection.

**Category-level Prompt Generation.** In parallel, we construct a category-level prompt bank containing general attributes relevant to each medical category. Using a language model like GPT-4, we generate detailed descriptions for common attributes such as shape, color, and morphology (e.g., “typical shapes of polyps include round, oval, and nodular-like”). This enriched prompt bank serves as a static reference, enabling the model to capture the broader context of each category and generalize effectively across diverse medical cases. Finally, we gather all attributes from the instance-level prompt and concatenate them with the GPT-4 augmented results to derive the category-level prompt (displayed in Appendix F).

**Application.** Category-level prompts provide comprehensive information for entire classes of medical images and remain fixed across all images within the same category, offering higher efficiency compared to instance-specific prompts. Despite this advantage, prior methods Guo et al. (2023); Qin et al. (2022); Wu et al. (2023b) have not fully benefited from general prompts (see Tab. 2) due to their lack of adaptive prompt selection. StructuralGLIP, however, utilizes an instance-wise selection mechanism that supports category-level prompts effectively. This allows the model to dynamically select the most relevant prompts from the prompt bank, achieving performance comparable to or even better than instance-level prompts on certain datasets. This demonstrates that our method can efficiently leverage general prompts to enhance zero-shot detection without the need for instance-specific generation.

## 4 EXPERIMENT

We illustrate our experiment settings in Fig. 2, where we design four distinct settings to evaluate the model’s performance. In Sec. 4.2, we follow traditional zero-shot setups to evaluate StructuralGLIP in a zero-shot setting without any fine-tuning on medical datasets, using both instance-specific and category-specific prompts (see Fig. 2(a) and (b)). In Sec. 4.3, we simulate clinical environments where supervised models are typically preferred. Here, we fine-tune the backbone of the proposed methods, *i.e.*, GLIP, (without using prompts) on medical datasets to form a refined detector. After fine-tuning, we incorporate linguistic prompts for the target disease into StructuralGLIP to perform

Table 1: Comparative experiment results on zero-shot medical detection across seven datasets, where **gray-shaded rows** represent the instance-level prompt results, while the unshaded rows represent the category-level prompt results.

Methods	CVC-300		Kvasir		ColonDB		ClinicDB		ETIS		ISIC 2016		BCCD		Avg.	
	AP	AP50														
GLIP	29.8	37.9	25.9	33.6	21.7	32.4	22.1	29.6	6.7	9.7	10.5	20.0	8.9	18.4	17.9	25.9
MIU-VL	36.5	66.6	28.7	36.6	19.8	35.6	28.2	<b>40.6</b>	9.4	15.4	21.7	35.7	11.4	20.4	22.2	35.8
AutoPrompter	52.7	70.6	30.4	39.7	31.9	45.9	22.0	30.6	17.7	26.5	19.9	32.9	12.9	22.3	26.7	38.3
Ours (instance)	<b>54.3</b>	<b>72.8</b>	<b>34.7</b>	<b>43.1</b>	<b>35.3</b>	<b>51.3</b>	<b>28.6</b>	38.2	<b>22.2</b>	<b>31.9</b>	<b>27.7</b>	<b>40.8</b>	<b>13.5</b>	<b>24.1</b>	<b>30.9</b>	<b>43.1</b>
MPT w. WBF	3.27	9.40	12.2	14.4	14.2	19.1	11.2	14.0	12.0	17.0	1.13	5.37	1.22	4.75	7.8	12.0
MPT w. Cluster	36.7	47.5	12.0	17.0	11.9	21.4	11.2	14.0	12.0	17.0	19.8	30.9	14.3	33.8	16.8	25.9
Ours (category)	<b>63.9</b>	<b>89.8</b>	<b>42.0</b>	<b>50.5</b>	<b>42.1</b>	<b>66.0</b>	<b>42.0</b>	<b>57.0</b>	<b>30.4</b>	<b>40.3</b>	<b>21.8</b>	<b>33.5</b>	<b>23.6</b>	<b>40.9</b>	<b>37.9</b>	<b>54.0</b>

zero-shot enhancement, evaluating the model’s ability to improve performance even after fine-tuning (see Fig. 2(c) and (d)). The fine-tuned details are provided in Appendix C.

#### 4.1 EXPERIMENTAL SETUP

**Datasets.** We select four types of medical imaging datasets involving eight benchmarks: 1) Endoscopy datasets for polyp detection: ClinicDB Bernal et al. (2015); Fernández-Esparrach et al. (2016), ColonDB Bernal et al. (2012), Kvasir Jha et al. (2020), ETIS Silva et al. (2014); 2) Microscopy dataset: BCCD shenggan et al. (2018) for blood cells detection; 3) Photography dataset: ISIC-2016 for skin lesions detection (benign lesion; malignant lesion); 4) Radiology image datasets: TBX11K Liu et al. (2023b) for tuberculosis detection in lung X-rays. Detailed elaboration is given in the Appendix B.

**Metric and baseline.** To evaluate our approach, we primarily benchmark against recent studies, mainly following Qin *et al.* Qin et al. (2022) (2023) and Wu *et al.* Wu et al. (2023b) (2023). Our baselines include recent GLIP-based methods (vanilla GLIP Li et al. (2022b), MIU-VL Qin et al. (2022), and AutoPrompter Wu et al. (2023b)) for instance-specific prompt generation setting, and works attempt to use category-specific prompt for detection (MPT Guo et al. (2023), and its variants MPT+SoftNMS Bodla et al. (2017), MPT+WBF Solovyev et al. (2021)). For zero-shot enhancement experiments, fully supervised detection models (RetinaNet Lin et al. (2020) and DyHead Dai et al. (2021)) are also included to provide a comprehensive evaluation landscape for our zero-shot enhancement experiments. The training details of the GLIP are elaborated in Appendix C.

#### 4.2 RESULTS OF ZERO-SHOT MEDICAL DETECTION

**Superior transfer performance across various medical scenarios.** *For fairness, we ensured that all methods used consistent prompts for a fair comparison.* For instance-specific prompt methods, we utilized BLIP (Li et al., 2022a) as the vision-question answering model for all approaches, except for vanilla GLIP (Li et al., 2022b), which directly used the target name as text input. For MIU-VL (Qin et al., 2022), we additionally used PubMedBert Gu et al. (2021) to generate prompts specific to the target disease. AutoPrompter (Wu et al., 2023b) uses GLIP to produce the initial bounding box with instance-specific prompt and refine them with a self-training process with Yolo-X (Zheng et al., 2021). The experimental results are shown in Tab. 1 (instance-specific prompt), where all prompt methods enhance the original GLIP model’s performance by providing additional descriptions. Among them, StructuralGLIP achieved the greatest improvement, with an average +4.2% AP  $\uparrow$ , +4.8% AP50  $\uparrow$  across seven datasets. We do not exhibit the results for the radiology dataset TBX-11k here, as the initial performance of the GLIP model on this dataset was poor, and the performance improvement for each prompt method is not distinguishable.

Table 2: AP% of vanilla GLIP and the proposed methods with instance-specific (I) and category-specific (C) prompt under zero-shot detection setting.

	CVC-300		ClinicDB		Kvasir		Avg.	
	C	I	C	I	C	I	C	I
GLIP	34.3	29.8	17.9	22.1	22.3	25.9	24.8	25.9
ours	<b>63.9</b>	<b>54.3</b>	<b>42.0</b>	<b>28.6</b>	<b>42.0</b>	<b>34.9</b>	<b>48.3</b>	<b>39.2</b>

Table 3: AP% of fine-tuned GLIP and the proposed methods with instance-specific (I) and category-specific (C) prompt under zero-shot enhancement setting.

	CVC-300		ClinicDB		Kvasir		Avg.	
	C	I	C	I	C	I	C	I
GLIP	70.0	67.5	54.3	63.0	44.5	51.1	56.2	60.5
ours	<b>77.2</b>	<b>74.9</b>	<b>70.4</b>	<b>68.4</b>	<b>71.3</b>	<b>69.6</b>	<b>72.9</b>	<b>70.9</b>

**Knowledge bank facilitates category-level prompts.** In this experiment, we focus on the effectiveness of category-level prompts generated by BLIP and GPT-4, which expand attributes related to the target across different dimensions such as colors, shapes, textures, and locations. These category-level prompts, being about 10 times longer than instance-specific prompts, remain consistent across all instances within the same class, and their details are provided in Appendix F. To benchmark against other methods, we include the MPT (Guo et al., 2023) approach, which is built upon the GLIP backbone and designed specifically to handle category-level prompts. MPT employs different prompt ensemble strategies, such as Weighted Box Fusion (WBF) and clustering, to split the category prompts into multiple groups and fuse the outputs for improved performance. Table 1 shows the performance comparison under different ensemble strategies. As seen in the results, StructuralGLIP achieves superior average performance across seven datasets compared to MPT. More importantly, StructuralGLIP consistently outperforms instance-specific prompt methods when utilizing category-level prompts (a +7% average AP  $\uparrow$  across seven datasets). This suggests that StructuralGLIP can effectively harness the richer and more comprehensive information encoded in the category prompts.

We attribute this advantage to the dual-branch architecture of StructuralGLIP, where the prompts and image features are separated into an auxiliary and main branch, respectively. By introducing an instance-wise selection mechanism, StructuralGLIP can dynamically select the most relevant parts of the category prompt based on the input image. To further verify this, we directly feed the category prompt for GLIP to obtain GLIP’s performance under the category prompt and follow MIU-VL to obtain its performance under the instance prompt, As shown in Table 2. The results demonstrate a significant improvement (average AP of 24.8  $\rightarrow$  49.3) in StructuralGLIP’s performance compared to the vanilla GLIP with category-level prompts. Interestingly, by comparing the performance of GLIP between using category-level prompt (see Tab. 2) and instance-level prompt (see Tab. 1), vanilla GLIP exhibit performance degradation when category prompts are employed (average AP of 25.7  $\rightarrow$  24.8). In contrast, StructuralGLIP shows a significant AP improvement (39.2  $\rightarrow$  49.3). This highlights the advantage of StructuralGLIP’s knowledge modeling and its ability to dynamically extract the most relevant prompt information for each instance, effectively leveraging the comprehensive knowledge provided by category-level prompts.

#### 4.3 RESULTS OF ZERO-SHOT ENHANCEMENT FOR MEDICAL DETECTION

**StructuralGLIP surpasses the fully-supervised methods.** In this experiment, we evaluate zero-shot enhancement and also compare fine-tuned GLIP-based models with classic object detection models, such as FasterRCNN Ren et al. (2015) and RetinaNet Lin et al. (2020), which were fully supervised. As shown in Tab. 4, while the refined GLIP performs similarly to the supervised RetinaNet (55.2 vs. 56.6 average AP), incorporating instance-level prompts with StructuralGLIP raises the performance to 59.3 AP, a notable +2.7% improvement. For category-level prompts, StructuralGLIP achieves an average AP of 60.6, showing a slight improvement over instance-level prompts. However, *given that category-level prompts remain fixed across all images of the same class and can be pre-encoded in our auxiliary branch*, this performance boost comes with only the inference cost for calculating the attention matrix of prompt, further demonstrating the efficiency of our approach.

**StructuralGLIP facilitates further improvement on fine-tuned models.** Interestingly, we observe that not all prompt-based methods effectively enhance a fine-tuned GLIP model. As shown in Tab. 4, methods like MIU-VL and AutoPrompter experience performance degradation when applied to the refined GLIP (MIU-VL: 56.6  $\rightarrow$  50.7 AP, AutoPrompter: 56.6  $\rightarrow$  53.3 AP). This decline likely occurs because these methods treat prompts as simple contextual information for the target name. During

Table 4: Comparative zero-shot enhancement experiment results across datasets, s, where **gray-shaded rows** represent the instance-level prompt results, while the last unshaded block represents the category-level prompt results.

Methods	Kvasir		ColonDB		ClinicDB		ETIS		CVC-300		ISIC 2016		BCCD		TBX-11k	
	AP	AP50														
FasterRCNN	63.4	-	44.1	-	71.6	-	44.5	-	59.4	-	50.3	-	56.9	-	33.9	73.9
RetinaNet	64.1	-	49.8	-	71.9	-	46.6	-	61.6	-	<b>54.0</b>	-	56.7	-	37.0	77.9
GLIP	64.8	82.2	56.8	79.1	65.1	82.6	60.4	77.0	75.2	95.9	39.9	50.9	55.4	78.2	35.2	75.3
MIU-VL	67.7	86.2	48.8	75.2	63.0	82.6	48.9	68.8	67.5	<b>97.2</b>	29.7	38.7	44.5	58.9	35.5	76.7
AutoPrompter	<b>70.0</b>	87.5	57.8	<b>81.3</b>	67.5	85.3	59.6	76.8	<b>75.2</b>	97.1	37.3	49.0	23.4	33.2	35.7	76.5
Ours (instance)	69.6	<b>87.9</b>	<b>58.1</b>	81.0	<b>68.4</b>	<b>87.5</b>	<b>60.3</b>	<b>77.0</b>	74.9	96.3	49.5	<b>62.7</b>	<b>56.9</b>	<b>80.2</b>	<b>37.3</b>	<b>78.2</b>
MPT+Cluster	25.1	30.0	22.3	29.5	24.8	29.3	24.7	29.8	33.4	41.5	25.6	33.7	22.8	30.6	31.4	68.2
Ours (category)	<b>71.3</b>	<b>89.0</b>	<b>62.0</b>	<b>85.3</b>	<b>70.4</b>	<b>88.2</b>	<b>62.4</b>	<b>79.5</b>	<b>77.2</b>	<b>96.5</b>	45.9	<b>58.3</b>	<b>57.8</b>	<b>82.4</b>	<b>37.8</b>	<b>79.2</b>

Table 5: Ablation results for Top-Q (y-axis) and Top-P (x-axis) on CVC-300 dataset with zero-shot medical detection setting.

5	15.1	50.1	53.4	52.4	52.4	51.9	52.4
10	19.9	47.1	56.5	55.9	55.3	55.5	55.8
15	19.9	47.1	56.0	55.4	54.9	55.2	55.3
20	17.3	48.2	55.2	54.9	54.9	54.9	55.2
30	18.8	50.4	56.4	55.6	55.9	56.1	56.1
40	17.9	50.2	56.1	55.1	54.9	55.8	56.2
	1	5	10	15	20	30	40

Table 6: Ablation study results (AP%) on the generation of category prompt using VQA and GPT across four datasets.

Methods	Kvasir	ColonDB	ClinicDB	ETIS
MPT+VQA+GPT	12.2	14.2	11.2	12.0
Ours+VQA	37.6	38.9	38.8	26.3
Ours+VQA+GPT	<b>42.0</b>	<b>42.1</b>	<b>42.0</b>	<b>30.4</b>

fine-tuning, only the target name is used as the linguistic input, causing a significant distribution shift when prompts are introduced during inference. In contrast, StructuralGLIP encodes prompts into a latent knowledge bank via the auxiliary branch, where prompts are used to construct structural representations during vision-language fusion. However, the final RPN inference still relies on the target name representation. In this way, StructuralGLIP incorporates additional knowledge about the target and alleviates the distribution shifting problem at the same time. This approach allows StructuralGLIP to achieve further performance gains on fine-tuned GLIP (56.6  $\rightarrow$  59.3 AP).

#### 4.4 ABLATION AND ANALYSIS

**Prompt as Knowledge Bank.** StructuralGLIP uses a dual-branch architecture and mutual selection mechanism to encode prompts into a latent knowledge bank, effectively supporting category-level prompts with rich attribute knowledge. To validate this, we directly feed category-level prompts of StructuralGLIP and instance-level prompt of MIU-VL for a vanilla GLIP to gain its performance with category-level prompt and instance-level prompt, respectively. As shown in Tab. 2, when employing category-level prompt, GLIP suffers a performance degradation (25.9 $\rightarrow$ 24.8) while StructuralGLIP gains additional performance improvement (39.2 $\rightarrow$ 48.3). This indicates that mutual selection helps StructuralGLIP effectively leverage category prompts by selecting the most relevant information for each image.

Another advantage of embedding prompts as a knowledge bank is that this design enables the precise integration of additional knowledge without affecting the distribution of the target representation. To validate this, we conducted ablation studies on the fine-tuned GLIP model, where only the target name is used during the training phase. Then, we evaluate the performance of GLIP and StructuralGLIP under a zero-shot enhancement setting. We present the experimental result in Tab. 3.

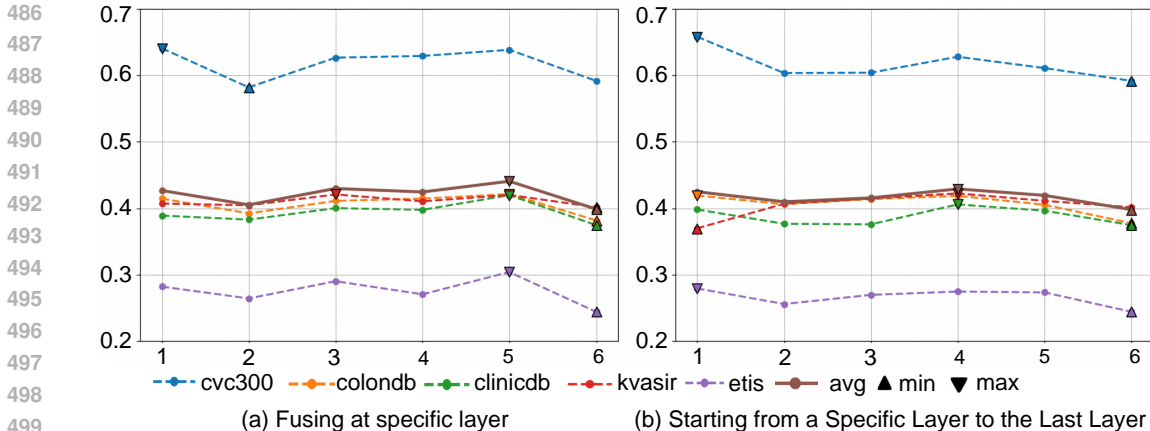


Figure 4: Ablation towards the fusing layer of the proposed method

Similar to the analysis in Tab. 2, the proposed StructuralGLIP effectively incorporates the knowledge from the bank without a performance degradation. As discussed in Sec. 4.3, with dual-branch architecture, the knowledge bank functions as a residual feature in the modality fusing phase, which prevents the distribution shift by encoding prompts separately from the target representation, ensuring smooth integration of prompt knowledge during inference.

**Category-prompt generation methods.** To validate the effectiveness of incorporating the prompt generated with the large language model, we exhibit the comparison of only using the VQA model and combining the results of VQA and GPT without fine-tuning the GLIP model in Tab. 4.4. Our experimental results show that GPT can provide more comprehensive knowledge about the target and further improve the performance.

**Ablation on  $Q$  and  $P$ .** We explore the joint effects of hyper-parameters of the selected visual tokens and prompt numbers  $Q$  and  $P$  on CVC-300 under zero-shot detection without the fine-tuned model. As shown in Tab. 4.4, the model achieves the optimal performance with  $P = 10$  and  $Q = 10$ . Further increasing  $P$  or  $Q$  introduces redundant information and degrades performance.

**Ablation on the fusing layer.** We performed an ablation study to analyze how the layer at which the latent knowledge bank is fused impacts the performance. Fig. 4 illustrates two fusion strategies. The first strategy, shown in Fig. 4(a), explores the effect of fusing at specific layers. The results indicate that fusion at Layer 5 yields the highest performance across multiple datasets, suggesting that this layer contains the most relevant features for effectively incorporating prompt knowledge. In contrast, earlier layers such as Layer 1 and Layer 2 exhibit lower performance, likely due to their focus on low-level features that are less compatible with the semantic richness of the prompts.

The second strategy, depicted in Figure 4(b), investigates the effect of starting from a specific layer and fusing through to the last layer (Layer 6). The results reveal a hierarchical pattern (Fusing Layer4-Layer5>Layer6>Layer6), where starting fusion from Layer 4 and continuing to Layer 6 achieves the best results. This indicates a progressively integrating the prompt knowledge at deeper layers allows the model to better utilize the information from the knowledge bank, rather than directly fusing at the last layer. A further analysis of this hierarchy characteristic is conducted in Appendix D, and more insights into the improvement of StructuralGLIP are shown in Appendix G.

## 5 CONCLUSION AND LIMITATION

We introduced StructuralGLIP, a novel zero-shot medical detection model that achieves fine-grained alignment between target descriptions and medical images. Unlike prior works that directly transfer vision-language models to the medical domain, we extended zero-shot medical detection to a more practical setting by exploring both category-level prompts and zero-shot enhancement. Through extensive experiments, we demonstrated that StructuralGLIP excels under these conditions, significantly outperforming existing methods. In future work, we aim to extend the applicability of StructuralGLIP to more diverse medical and non-medical domains, potentially improving its adaptability to varied visual conditions and more complex multimodal tasks.

## REFERENCES

- 540  
541  
542 Josh Achiam, Steven Adler, Sandhini Agarwal, Lama Ahmad, Ilge Akkaya, Florencia Leoni Aleman,  
543 Diogo Almeida, Janko Altenschmidt, Sam Altman, Shyamal Anadkat, et al. Gpt-4 technical report.  
544 *arXiv preprint arXiv:2303.08774*, 2023.
- 545 Maged Badawi, Mohammedyahaia Abushanab, Sheethal Bhat, and Andreas Maier. Review of zero-  
546 shot and few-shot ai algorithms in the medical domain. *arXiv preprint arXiv:2406.16143*, 2024.  
547
- 548 Ankan Bansal, Karan Sikka, Gaurav Sharma, Rama Chellappa, and Ajay Divakaran. Zero-shot  
549 pediatric tuberculosis detection in chest x-rays using self-supervised learning. In *ISBI*, 2024.
- 550 Jorge Bernal, Javier Sánchez, and Fernando Vilarino. Towards automatic polyp detection with a  
551 polyp appearance model. *Pattern Recognition*, 45(9):3166–3182, 2012.  
552
- 553 Jorge Bernal, F Javier Sánchez, Gloria Fernández-Esparrach, Debora Gil, Cristina Rodríguez, and  
554 Fernando Vilariño. Wm-dova maps for accurate polyp highlighting in colonoscopy: Validation vs.  
555 saliency maps from physicians. *Computerized medical imaging and graphics*, 43:99–111, 2015.
- 556 Yanchao Bi. Dual coding of knowledge in the human brain. *Trends in Cognitive Sciences*, 25(10):  
557 883–895, 2021.  
558
- 559 Cheng Bian, Chenglang Yuan, Kai Ma, Shuang Yu, Dong Wei, and Yefeng Zheng. Domain adaptation  
560 meets zero-shot learning: An annotation-efficient approach to multi-modality medical image  
561 segmentation. *IEEE Transactions on Medical Imaging*, 41(5):1043–1056, 2022. doi: 10.1109/  
562 TMI.2021.3131245.
- 563 Navaneeth Bodla, Bharat Singh, Rama Chellappa, and Larry S Davis. Soft-nms—improving object  
564 detection with one line of code. In *ICCV*, pp. 5561–5569, 2017.  
565
- 566 Xiyang Dai, Yinpeng Chen, Bin Xiao, Dongdong Chen, Mengchen Liu, Lu Yuan, and Lei Zhang.  
567 Dynamic head: Unifying object detection heads with attentions. In *CVPR*, pp. 7373–7382, 2021.  
568
- 569 Yu Du, Fangyun Wei, Zihe Zhang, Miaojing Shi, Yue Gao, and Guoqi Li. Learning to prompt for  
570 open-vocabulary object detection with vision-language model. In *CVPR*, pp. 14084–14093, 2022.
- 571 Glòria Fernández-Esparrach, Jorge Bernal, María López-Cerón, Henry Córdova, Cristina Sánchez-  
572 Montes, Cristina Rodríguez De Miguel, and Francisco Javier Sánchez. Exploring the clinical  
573 potential of an automatic colonic polyp detection method based on the creation of energy maps.  
574 *Endoscopy*, pp. 837–842, 2016.
- 575 Yu Gu, Robert Tinn, Hao Cheng, Michael Lucas, Naoto Usuyama, Xiaodong Liu, Tristan Naumann,  
576 Jianfeng Gao, and Hoifung Poon. Domain-specific language model pretraining for biomedical  
577 natural language processing. *ACM Transactions on Computing for Healthcare (HEALTH)*, 3(1):  
578 1–23, 2021.  
579
- 580 Miaotian Guo, Huahui Yi, Ziyuan Qin, Haiying Wang, Aidong Men, and Qicheng Lao. Multiple  
581 prompt fusion for zero-shot lesion detection using vision-language models. In *MICCAI*, pp.  
582 283–292, 2023.
- 583 Debesh Jha, Pia H Smedsrud, Michael A Riegler, Pål Halvorsen, Thomas De Lange, Dag Johansen,  
584 and Håvard D Johansen. Kvasir-seg: A segmented polyp dataset. In *MMM*, pp. 451–462, 2020.  
585
- 586 Diederik P Kingma and Jimmy Ba. Adam: A method for stochastic optimization. *arXiv preprint*  
587 *arXiv:1412.6980*, 2014.
- 588 Haoran Lai, Qingsong Yao, Zihang Jiang, Rongsheng Wang, Zhiyang He, Xiaodong Tao, and S Kevin  
589 Zhou. Carzero: Cross-attention alignment for radiology zero-shot classification. In *CVPR*, pp.  
590 11137–11146, 2024.  
591
- 592 Loïc Le Bescond, Marvin Lerousseau, Ingrid Garberis, Fabrice André, Stergios Christodoulidis, Maria  
593 Vakalopoulou, and Hugues Talbot. Unsupervised nuclei segmentation using spatial organization  
priors. In *MICCAI*, pp. 325–335, 2022.

- 594 Junnan Li, Dongxu Li, Caiming Xiong, and Steven Hoi. Blip: Bootstrapping language-image pre-  
595 training for unified vision-language understanding and generation. In *ICML*, pp. 12888–12900,  
596 2022a.
- 597 Liunian Harold Li, Pengchuan Zhang, Haotian Zhang, Jianwei Yang, Chunyuan Li, Yiwu Zhong,  
598 Lijuan Wang, Lu Yuan, Lei Zhang, Jenq-Neng Hwang, et al. Grounded language-image pre-training.  
599 In *CVPR*, pp. 10965–10975, 2022b.
- 600 Liunian Harold Li, Pengchuan Zhang, Haotian Zhang, Jianwei Yang, Chunyuan Li, Yiwu Zhong,  
601 Lijuan Wang, Lu Yuan, Lei Zhang, Jenq-Neng Hwang, et al. Grounded language-image pre-training.  
602 In *CVPR*, pp. 10965–10975, 2022c.
- 603 Tsung-Yi Lin, Priya Goyal, Ross Girshick, Kaiming He, and Piotr Dollar. Focal loss for dense object  
604 detection. *IEEE transactions on pattern analysis and machine intelligence*, 42(2):318–327, 2020.
- 605 Jiaxiang Liu, Tianxiang Hu, Yan Zhang, Xiaotang Gai, YANG FENG, and Zuozhu Liu. A chatgpt  
606 aided explainable framework for zero-shot medical image diagnosis. In *ICML*, 2023a.
- 607 Yun Liu, Yu-Huan Wu, Shi-Chen Zhang, Li Liu, Min Wu, and Ming-Ming Cheng. Revisiting  
608 computer-aided tuberculosis diagnosis. *IEEE Transactions on Pattern Analysis and Machine  
609 Intelligence*, 2023b.
- 610 Ming Y Lu, Bowen Chen, Andrew Zhang, Drew FK Williamson, Richard J Chen, Tong Ding,  
611 Long Phi Le, Yung-Sung Chuang, and Faisal Mahmood. Visual language pretrained multiple  
612 instance zero-shot transfer for histopathology images. In *CVPR*, pp. 19764–19775, 2023.
- 613 Dwarikanath Mahapatra, Behzad Bozorgtabar, and Zongyuan Ge. Medical image classification using  
614 generalized zero shot learning. In *ICCV*, pp. 3344–3353, 2021.
- 615 Allan Paivio. *Imagery and verbal processes*. Psychology Press, 2013.
- 616 Angshuman Paul, Thomas C Shen, Sungwon Lee, Niranjana Balachandar, Yifan Peng, Zhiyong  
617 Lu, and Ronald M Summers. Generalized zero-shot chest x-ray diagnosis through trait-guided  
618 multi-view semantic embedding with self-training. *IEEE Transactions on Medical Imaging*, 40  
619 (10):2642–2655, 2021.
- 620 Vu Minh Hieu Phan, Yutong Xie, Yuankai Qi, Lingqiao Liu, Liyang Liu, Bowen Zhang, Zhibin Liao,  
621 Qi Wu, Minh-Son To, and Johan W. Verjans. Decomposing disease descriptions for enhanced  
622 pathology detection: A multi-aspect vision-language pre-training framework, 2024.
- 623 Ziyuan Qin, Hua Hui Yi, Qicheng Lao, and Kang Li. Medical image understanding with pretrained  
624 vision language models: A comprehensive study. In *ICLR*, 2022.
- 625 Shaoqing Ren, Kaiming He, Ross Girshick, and Jian Sun. Faster r-cnn: Towards real-time object  
626 detection with region proposal networks. *Advances in neural information processing systems*, 28,  
627 2015.
- 628 Mihir Sahasrabudhe, Stergios Christodoulidis, Roberto Salgado, Stefan Michiels, Sherene Loi,  
629 Fabrice André, Nikos Paragios, and Maria Vakalopoulou. Self-supervised nuclei segmentation in  
630 histopathological images using attention. In *MICCAI*, pp. 393–402, 2020.
- 631 shenggan, Nicolas Chen, cosmicad, and akshaylamba. Bccd: Blood cell count and detection, 2018.  
632 URL [https://github.com/Shenggan/BCCD\\_Dataset](https://github.com/Shenggan/BCCD_Dataset).
- 633 Juan Silva, Aymeric Histace, Olivier Romain, Xavier Dray, and Bertrand Granado. Toward embedded  
634 detection of polyps in wce images for early diagnosis of colorectal cancer. *International journal of  
635 computer assisted radiology and surgery*, 9:283–293, 2014.
- 636 James Seale Smith, Leonid Karlinsky, Vyshnavi Gutta, Paola Cascante-Bonilla, Donghyun Kim, Assaf  
637 Arbelle, Rameswar Panda, Rogerio Feris, and Zsolt Kira. Coda-prompt: Continual decomposed  
638 attention-based prompting for rehearsal-free continual learning. In *CVPR*, pp. 11909–11919, 2023.
- 639 Roman Solovyev, Weimin Wang, and Tatiana Gabruseva. Weighted boxes fusion: Ensembling boxes  
640 from different object detection models. *Image and Vision Computing*, 107:104117, 2021.

- 648 Ekin Tiu, Ellie Talius, Pujan Patel, Curtis P Langlotz, Andrew Y Ng, and Pranav Rajpurkar. Expert-  
649 level detection of pathologies from unannotated chest x-ray images via self-supervised learning.  
650 *Nature Biomedical Engineering*, 6(12):1399–1406, 2022.
- 651 Ashish Vaswani, Noam Shazeer, Niki Parmar, Jakob Uszkoreit, Llion Jones, Aidan N Gomez, Łukasz  
652 Kaiser, and Illia Polosukhin. Attention is all you need. *Advances in neural information processing*  
653 *systems*, 30, 2017.
- 654 Konstantinos Vilouras, Pedro Sanchez, Alison Q O’Neil, and Sotirios A Tsaftaris. Zero-shot medical  
655 phrase grounding with off-the-shelf diffusion models. *arXiv preprint arXiv:2404.12920*, 2024.
- 656 Runqi Wang, Xiaoyue Duan, Guoliang Kang, Jianzhuang Liu, Shaohui Lin, Songcen Xu, Jinhu Lü,  
657 and Baochang Zhang. Attriclip: A non-incremental learner for incremental knowledge learning. In  
658 *CVPR*, pp. 3654–3663, 2023.
- 659 Zifeng Wang, Zizhao Zhang, Sayna Ebrahimi, Ruoxi Sun, Han Zhang, Chen-Yu Lee, Xiaoqi Ren,  
660 Guolong Su, Vincent Perot, Jennifer Dy, et al. Dualprompt: Complementary prompting for  
661 rehearsal-free continual learning. In *ECCV*, pp. 631–648, 2022a.
- 662 Zifeng Wang, Zizhao Zhang, Chen-Yu Lee, Han Zhang, Ruoxi Sun, Xiaoqi Ren, Guolong Su, Vincent  
663 Perot, Jennifer Dy, and Tomas Pfister. Learning to prompt for continual learning. In *CVPR*, pp.  
664 139–149, 2022b.
- 665 Chaoyi Wu, Xiaoman Zhang, Ya Zhang, Yanfeng Wang, and Weidi Xie. Medklip: Medical knowledge  
666 enhanced language-image pre-training for x-ray diagnosis. In *CVPR*, pp. 21372–21383, 2023a.
- 667 Yongjian Wu, Yang Zhou, Jiya Saiyin, Bingzheng Wei, Maode Lai, Jianzhong Shou, Yubo Fan,  
668 and Yan Xu. Zero-shot nuclei detection via visual-language pre-trained models. In *MICCAI*, pp.  
669 693–703, 2023b.
- 670 Lewei Yao, Jianhua Han, Youpeng Wen, Xiaodan Liang, Dan Xu, Wei Zhang, Zhenguo Li, Chunjing  
671 Xu, and Hang Xu. Detclip: Dictionary-enriched visual-concept paralleled pre-training for open-  
672 world detection. *Advances in Neural Information Processing Systems*, 35:9125–9138, 2022.
- 673 Xiaoman Zhang, Chaoyi Wu, Ya Zhang, Weidi Xie, and Yanfeng Wang. Knowledge-enhanced  
674 visual-language pre-training on chest radiology images. *Nature Communications*, 14(1):4542,  
675 2023.
- 676 Ge Zheng, Liu Songtao, Wang Feng, Li Zeming, Sun Jian, et al. Yolox: Exceeding yolo series in  
677 2021. *arXiv preprint arXiv:2107.08430*, 2021.
- 678  
679  
680  
681  
682  
683  
684  
685  
686  
687  
688  
689  
690  
691  
692  
693  
694  
695  
696  
697  
698  
699  
700  
701

## A COMPARATIVE VISUALIZATION

We illustrate the detection results on the ColonDB and BCCD dataset in Fig. E, where we employ the vanilla GLIP for these prompt-based methods. Intuitively, both AutoPrompter and MIU-VL struggle with either over-detection or missing critical targets. This is likely due to the coarse alignment between vision and target representations, leading to false positives and missed detections. For example, in ColonDB, both methods produce inconsistent bounding boxes, failing to accurately localize the polyp. On the other hand, StructuralGLIP demonstrates more precise localization with category-level prompts, leading to fewer missed targets and improved confidence scores.

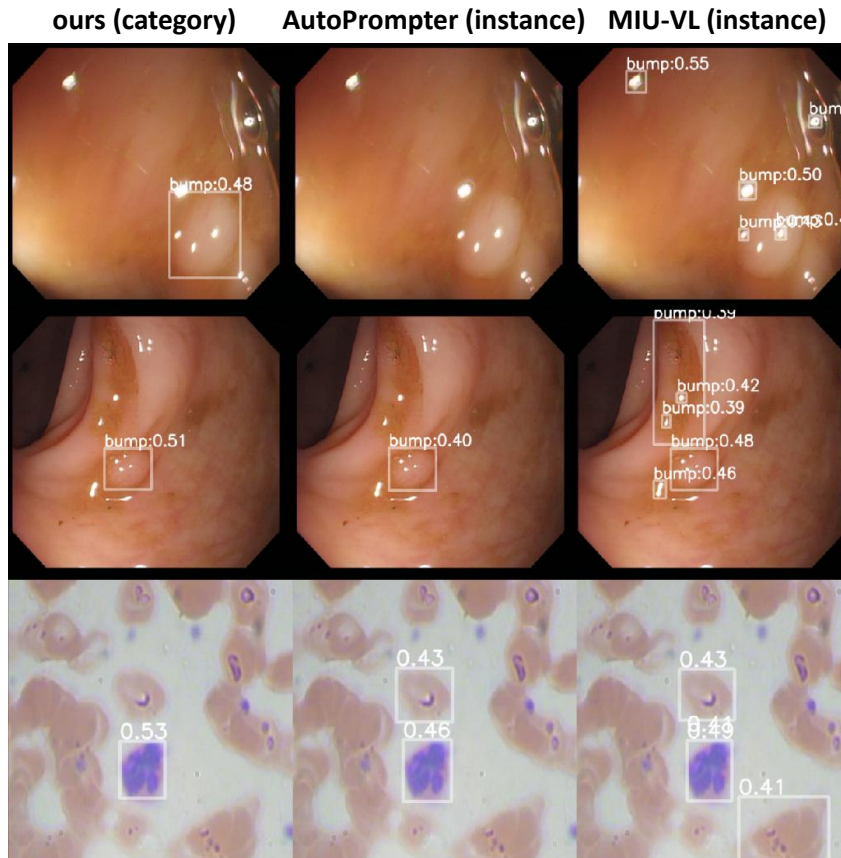


Figure A: Visualization Results on the ColonDB and BCCD datasets. We demonstrate example detection results on the ISIC2016 and TBX11K datasets in Fig. B below, where we employ the fine-tuned GLIP and AutoPrompter for comparison. As shown in Fig. B(a), it is evident that vanilla GLIP and AutoPrompter fail to produce correct classification results for lesion detection. In contrast, our method, benefiting from the category-level prompt, makes correct classification. For radiographic datasets, our instance method achieves higher confidence scores using the same prompts with AutoPrompter.

## B DATASET INTRODUCTION

We select four types of medical imaging datasets involving eight benchmarks:

1) Endoscopy datasets for polyp detection: ClinicDB Bernal et al. (2015); Fernández-Esparrach et al. (2016), ColonDB Bernal et al. (2012), Kvasir Jha et al. (2020), ETIS Silva et al. (2014). There are 2,248 images and 2,374 bboxes in total. The complete training and validation images for the entire benchmark are 1160 and 290, respectively. And the number of test set images for CVC-300, CVC-ClinicDB, CVC-ColonDB, Kvasir, and ETIS datasets are 60, 62, 380, 100, and 196 respectively.

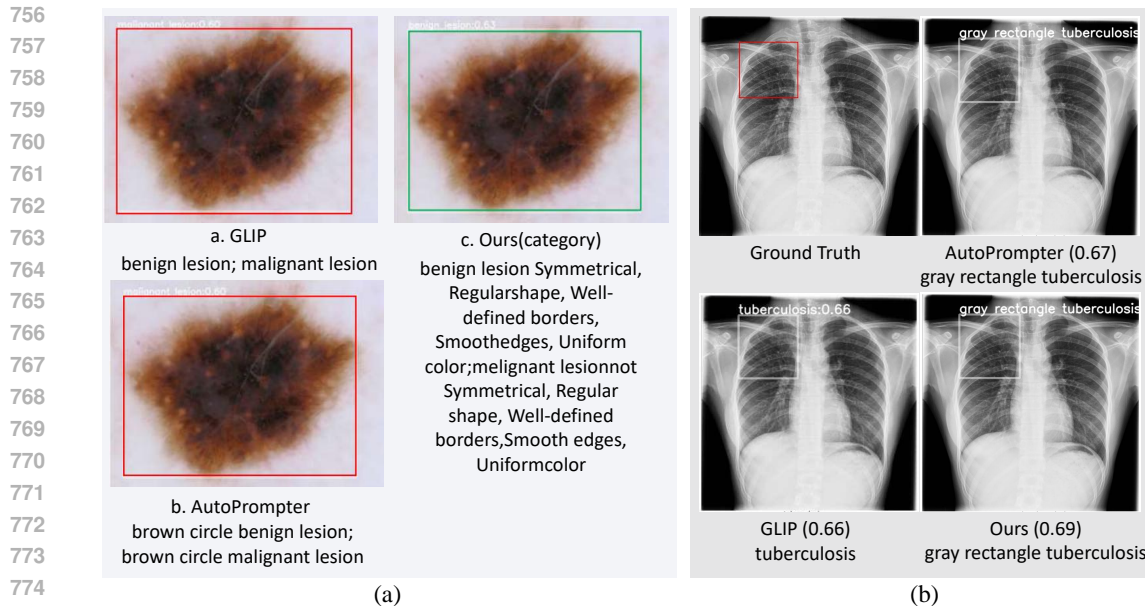


Figure B: Visualization Results on the ISIC2016 and TBX11K datasets.

The primary challenge involves highly variable polyp appearances, obscured views due to mucus and bleeding, and low contrast against surrounding tissues.

2) Microscopy dataset: BCCD shenggan et al. (2018) for blood cell detection (white blood cells, red blood cells, and platelets). The BCCD dataset is designed for blood cell detection tasks, including three classes: white blood cells, red blood cells, and platelets. There are 874 images with 11,789 bboxes for the entire BCCD dataset.

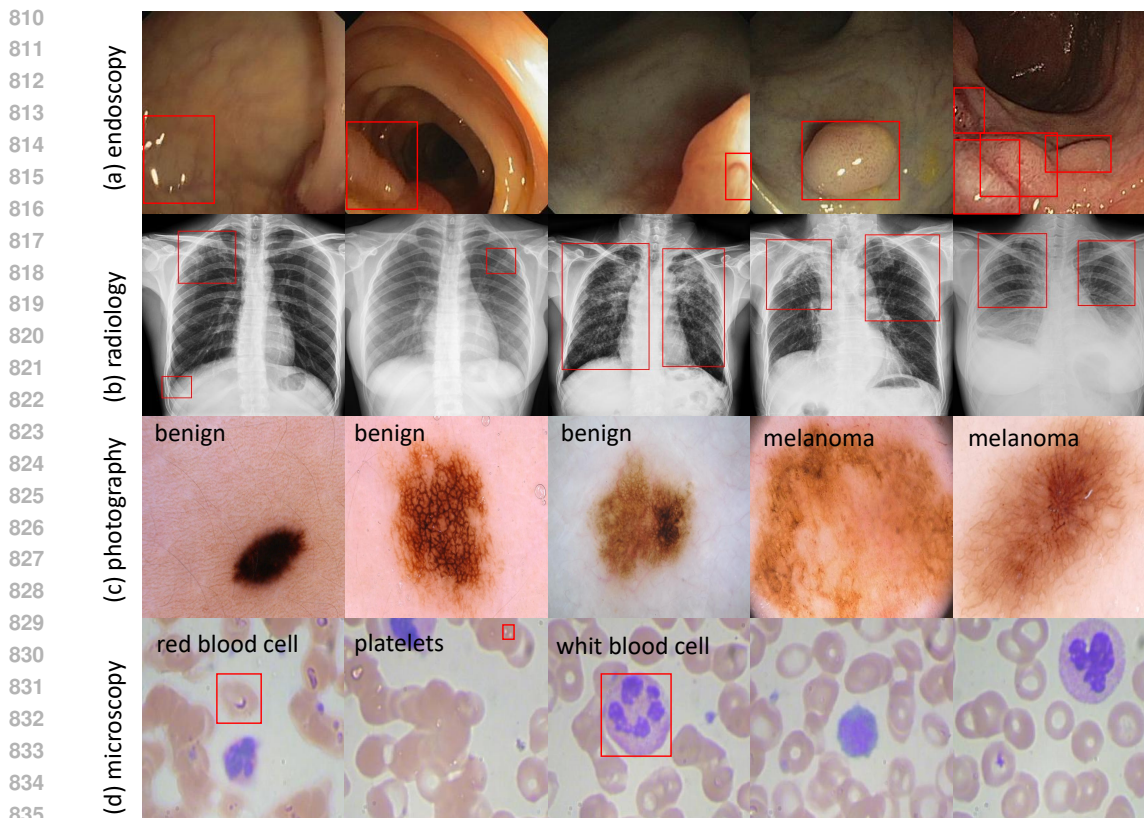
3) Photography dataset: ISIC-2016 for skin lesions detection (benign lesion, malignant lesion). The ISIC-16 dataset consists of 1,279 images with 1,282 bboxes for benign skin lesions and melanoma detection, divided into 720/180/379 images for training, validation, and testing. This dataset poses difficulties due to the small size and high density of the targets, and variations in staining which affect visual clarity and consistency.

4) Radiology image datasets: TBX11k Liu et al. (2023b) for tuberculosis detection in lung x-rays. These datasets are challenging due to the subtle nature of disease indicators, which can obscure key features. The TBX11K dataset is used for tuberculosis detection in the lung, including 799 images and 1,211 bbox labels. Moreover, this dataset is divided into 479/120/200 images for training, validation, and testing sets, respectively.

We demonstrate some example images of these datasets in Fig. F below.

## C TRAINING DETAILS FOR GLIP'S ZERO-SHOT ENHANCEMENT EXPERIMENT

The zero-shot enhancement aims to further improve the performance of models after supervised training on the downstream datasets. We follow Qin et al. (2022) to use a fine-tuned GLIP model optimized with the Adam optimizer Kingma & Ba (2014), where the initial learning rate is set to  $1 \times 10^{-4}$  ( $1 \times 10^{-5}$  for the BERT text encoder). A weight decay of 0.05 is applied to prevent overfitting, and the bottom two layers of the image encoder are frozen to preserve fundamental features. Our expressive prompts tailored to the characteristics of the target's appearance are generated using GPT-4 Achiam et al. (2023). Full details of these prompts are available in the Appendix.



837 Figure C: Examples of medical images under different imaging conditions.

838  
839 **D ANALYSIS FOR THE HIERARCHICAL CHARACTERISTIC OF THE**  
840 **STRUCTURAL REPRESENTATION.**  
841

842  
843 To validate the hierarchical nature of the structural representations derived through layer-wise prompt  
844 retrieval, we analyzed the distribution of selected prompts across six GLIP model encoder layers.  
845 Specifically, we conducted this analysis using StructuralGLIP with category-level prompts on two  
846 medical detection tasks: BCCD red blood cell detection and ClinicDB polyp detection. Prompts  
847 were categorized into four types: color, location, shape, and texture (see detailed prompt categories  
848 in Appendix F). The results, shown in Fig. D, reveal distinct differences in the frequency of selected  
849 prompt types across layers (see Tab. A for the concrete value of the figure). In both tasks, color  
850 prompts were consistently selected across all layers, highlighting its importance in medical detection.  
851 For ClinicDB, the frequency of shape and texture prompts increased in deeper layers, indicating that  
852 these features become more relevant as the model abstracts more complex attributes. In contrast, for  
853 red blood cell detection, color remains the predominant feature across layers, while the selection of  
854 shape and texture prompts decreases. This analysis demonstrates that StructuralGLIP can dynamically  
855 retrieve task-relevant prompts from the knowledge bank at different layers, confirming the adaptable  
856 nature of our zero-shot medical detection framework.

857 **E EFFECT OF PROMPT QUALITY.**  
858

859 As shown in Tab. B, we present the detailed target description (query name with prompt) for red  
860 blood cells detection task, and only using the category name “red blood cells” as input to the model  
861 of GLIP resulted in poor detection performance, with an AP of just 1.7%. From Tab. B, it is evident  
862 that the design of prompt methods significantly affects the ability of vision-language models to  
863 utilize prompts for domain enhancement. For instance, our method, with the simple prompt, “pink  
oval”, outperforms MIU-VL, which uses multiple types of attributes, achieving a +7.4%AP50 and

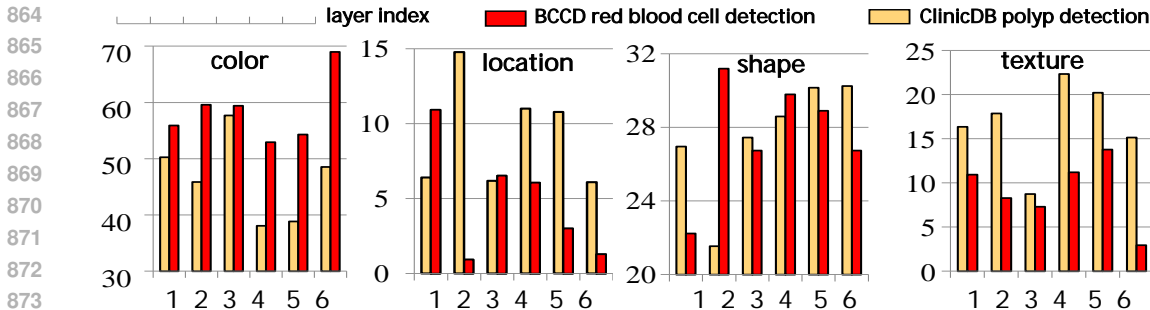


Figure D: Results of the selected frequency (y-axis) of different types of prompts across the network’s layer (x-axis).

Attribute	colors		locations		shapes		texture	
Dataset	polyp	red blood cell	polyp	red blood cell	polyp	red blood cell	polyp	red blood cell
layer1	1436	1192	183	233	770	474	467	233
layer2	1468	1073	473	17	690	562	572	149
layer3	1475	1109	158	122	702	499	223	136
layer4	1505	1160	436	133	1131	653	883	245
layer5	1498	1062	416	59	1163	565	779	269
layer6	1450	1117	182	21	904	433	452	48

Table A: The selected frequencies of different types of prompts across GLIP’s different layers

+4.3%AP improvement. This improvement is attributed to our structural representation, which achieves hierarchical vision-language alignment, thereby enhancing the utilization of prompts for medical image analysis. Additionally, the structural representation involves fine-grained vision-language alignment, enabling precise selection of attribute tokens from prompts. This capability allows our method to effectively incorporate more comprehensive prompts, leading to a further improvement of 5.1%AP50 based on the simple short prompt. This demonstrates the effectiveness and robustness of our approach in generating and utilizing prompts for zero-shot detection tasks, showcasing its superiority in achieving efficient and accurate medical image analysis.

Table B: Comparison of different methods with different prompts based on the red blood detection task of BCCD dataset (complete prompts are shown in Appendix F).

Methods	Target Description (name+prompt)	AP	AP50
GLIP	[name] red blood cells	1.7	4.3
MIU-VL	[name] + red color + spherical shape + in birth	12.0	24.7
AutoPrompter	[name] + pink oval	12.6	27.0
Ours	[name] + pink oval	<b>16.3</b>	<b>34.4</b>
MPT+Cluste	[name] + (four prompts below) [flesh-colored, pink, round, blood]	12.5	25.6
Ours (category)	[name]+ [color] pale bright, et al.+ [shape] oval round, et al. + [texture] smooth rough et al.+ [location] peripheral central, et al.	<b>19.3</b>	<b>39.5</b>

## F DETAILED CATEGORY-PROMPT FOR THE MEDICAL DATASETS

Colors	Shapes	Textures	Locations
--------	--------	----------	-----------

918  
919  
920  
921  
922  
923  
924  
925  
926  
927  
928  
929  
930  
931  
932  
933  
934  
935  
936  
937  
938  
939  
940  
941  
942  
943  
944  
945  
946  
947  
948  
949  
950  
951  
952  
953  
954  
955  
956  
957  
958  
959  
960  
961  
962  
963  
964  
965  
966  
967  
968  
969  
970  
971

Polyp	<i>white, yellow, orange, red, brown, pink, pale, tan, gray-white, gold, cream, ruby, turquoise, indigo, violet</i>	<i>octagon, circle, round, heart, oblong, oval, small, rounded, jagged, wide, large, bulbous, spherical, circular, irregular, diamond</i>	<i>smooth, textured, cracked, striped, shiny, dull, speckled, raised, rough, granular, grooved, glossy, veined, pigmented, uneven, mottled, interwoven, lines, patches, complex, reticular, structure</i>	<i>rectal, mucosal, elevated, demarcated, creased, folded, isolated, clustered, solitary, honeycombed</i>
Red Blood Cells	<i>pale, bright red, dark red, pinkish, crimson, ruby, coral, salmon, cherry, scarlet, rusty, maroon, wine, burgundy, rosy, flamingo, peach, copper, mahogany, terracotta</i>	<i>disc-shaped, oval, round, elongated, spherical, ring-like, bean-shaped, crescent, irregular, biconcave, elliptical, cuboidal, triangular, squamous, fusiform, polygonal, rod-shaped, fibrillar, amorphous, lobed</i>	<i>smooth, rough, granular, fibrous, glossy, matte, sticky, velvety, spongy, creased, crystalline, jelly-like, pitted, wrinkled, spiny, bumpy, flaky, mucous, papillary, striated</i>	<i>peripheral, central, upper, lower, medial, lateral, distal, proximal, anterior, posterior, cervical, thoracic, abdominal, pelvic, inguinal, axillary, oral, nasal, occipital parietal</i>
White Blood Cells	<i>purple, white, pink, gray, blue, translucent, lavender, milky, yellow, pale, clear, light purple, ivory, cream, faint blue, silver, off-white, light gray, opalescent</i>	<i>round, oval, irregular, lobed, segmented, spherical, kidney-shaped, amoeboid, polymorphous, triangular, elongated, bean-shaped, cuboidal, crescent, spindle-shaped, fusiform, irregularly-shaped, star-shaped, flattened, discoid</i>	<i>granular, rough, smooth, wrinkled, spongy, matte, glossy, fibrous, pitted, veined, speckled, raised, lobulated, ridged, reticular, grooved, folded, striated, flaky, nodular, uneven</i>	<i>circulating, peripheral, thoracic, abdominal, pelvic, cervical, axillary, lymphatic, spleen, marrow, mediastinal, proximal, distal, inguinal, occipital, parietal, cranial, vertebral, lumbar, sacral</i>
Platelets	<i>yellow, gray, pink, translucent, clear, beige, orange, white, pale yellow, light gray, light pink, golden, amber, straw, ivory, light orange, peach, tan, light brown, opalescent</i>	<i>small, round, oval, irregular, disc-shaped, spiked, star-shaped, elongated, granular, fragmented, jagged, ring-shaped, crescent, cuboidal, polygonal, fibrillar, amorphous, fusiform, spherical, irregularly-shaped</i>	<i>granular, smooth, rough, spongy, fibrous, pitted, wrinkled, matte, glossy, veined, lobulated, striated, flaky, nodular, reticular, ridged, bumpy, raised, speckled, uneven, lumpy</i>	<i>circulating, peripheral, marrow, spleen, liver, thoracic, abdominal, lymphatic, distal, proximal, cervical, axillary, cranial, vertebral, sacral, pelvic, mediastinal, inguinal, parietal, occipital</i>
Benign Lesion	<i>light brown, tan, pale pink, beige, ivory, light yellow, flesh-colored, clear, translucent, white, pink, light red, off-white, cream, soft yellow, gray, peach, faint brown, faint yellow, light orange</i>	<i>round, oval, smooth-edged, well-defined, regular, flat, slightly raised, small, lobulated, dome-shaped, circular, symmetrical, uniform, elongated, flat-topped, irregular, semi-spherical, oblong, disc-shaped, heart-shaped</i>	<i>smooth, glossy, matte, uniform, fine, clear, unbroken, even, polished, soft, thin, flat, reticular, striated, nodular, shallow, granular, homogeneous, light-textured, delicate</i>	<i>superficial, epidermal, dermal, non-invasive, isolated, peripheral, central, facial, limb, torso, scalp, back, upper, lower, anterior, posterior, lateral, abdominal, neck, arm</i>

972					
973	Malignant	<i>dark brown, black, red, purple, blue,</i>	<i>irregular, asymmetric, poorly-defined, multi-lobed, jagged, raised, ulcerated, irregular-edged, large, deep, multi-colored, nodular, star-shaped, rough-edged, uneven, angular, oblong, rough, distorted, fragmented</i>	<i>rough, scaly, granular, ulcerated, cracked, irregular, firm, thick, pitted, fibrous, bumpy, crusty, glossy, uneven, speckled, reticular, indurated, papillary, pigmented, veined</i>	<i>invasive, dermal, subcutaneous, nodal, systemic, spread, clustered, axial, limb, facial, scalp, back, chest, abdominal, upper, lower, lateral, posterior, anterior, proximal, distal</i>
974	Lesion	<i>gray, deep red, maroon, dark purple, crimson, burgundy, dark gray, navy, violet, yellowish, pale gray, dark pink, reddish-brown, orange, tan</i>			
975					
976					
977					
978					
979					
980					
981					
982					
983					
984					
985	Tuberculosis	<i>white, gray, patchy, cloudy, translucent, opaque, pale, faint, bright, shadowed, dull, smoky, hazy, diffused, misty, dense, light gray, speckled, milky, gray-white</i>	<i>irregular, nodular, patchy, lobular, diffuse, multi-focal, rounded, asymmetrical, large, small, streaked, segmented, thickened, elongated, fragmented, scattered, spotty, uneven, consolidated, granular</i>	<i>rough, fibrotic, granular, nodular, scarred, thick, textured, coarse, uneven, reticular, banded, streaked, fibrous, pitted, grooved, layered, striated, indurated, dense, veined</i>	<i>apical, upper lobe, lower lobe, central, peripheral, posterior, anterior, lateral, mediastinal, pleural, diaphragmatic, tracheal, hilum, bronchiolar, thoracic, cervical, upper, lower, rib, clavicle</i>
986					
987					
988					
989					
990					
991					
992					
993					
994					
995					
996					

## 997 G ANALYSIS TOWARDS THE FEATURE DISTRIBUTION OF STRUCTURALGLIP.

999 To provide more insight into the improvement brought by StructuralGLIP, we focus on vision  
1000 and language features input into the RPN detection model before and after applying our proposed  
1001 approach. We conduct experiments on five datasets (cvc300, colondb, clinicdb, kvasir, etis) on the  
1002 vanilla GLIP without fine-tuning and calculate the average value of vision and target representation's  
1003 attention matrix (termed "average attention strength"). The prompt we used is category-level prompt.  
1004 Then, we employ a kernel density estimation method to estimate the distribution of average attention  
1005 strength. We found that there is a significant increase in average attention strength for the proposed  
1006 StructuralGLIP compared with the vanilla GLIP, indicating better alignment between vision and  
1007 language representations.

## 1009 H VISUALIZATION ON NATURAL IMAGES

1011 Here we demonstrate the visualization of the proposed StructuralGLIP and GLIP on natural images.  
1012 The prompt for each category is as follows:

- 1014 1. Cosmos: broad, delicate, slightly ruffled petals radiating symmetrically around a vibrant  
1015 yellow center, with a lightweight and airy appearance that contrasts beautifully against the  
1016 surrounding colors
- 1017 2. Peony: lush, voluminous, soft, delicate, vibrant, radiant, layered, rounded, ruffled, full,  
1018 graceful, elegant, eye-catching, rich, luxurious, intricate, symmetrical, silky, and captivating
- 1019 3. Hematite: flat and irregularly shaped, with a coarse and slightly grainy surface indicative of  
1020 its iron-rich composition

1021  
1022  
1023  
1024  
1025

1026  
1027  
1028  
1029  
1030  
1031  
1032  
1033  
1034  
1035  
1036  
1037  
1038  
1039  
1040  
1041  
1042  
1043  
1044  
1045  
1046  
1047  
1048  
1049  
1050  
1051  
1052  
1053  
1054  
1055  
1056  
1057  
1058  
1059  
1060  
1061  
1062  
1063  
1064  
1065  
1066  
1067  
1068  
1069  
1070  
1071  
1072  
1073  
1074  
1075  
1076  
1077  
1078  
1079

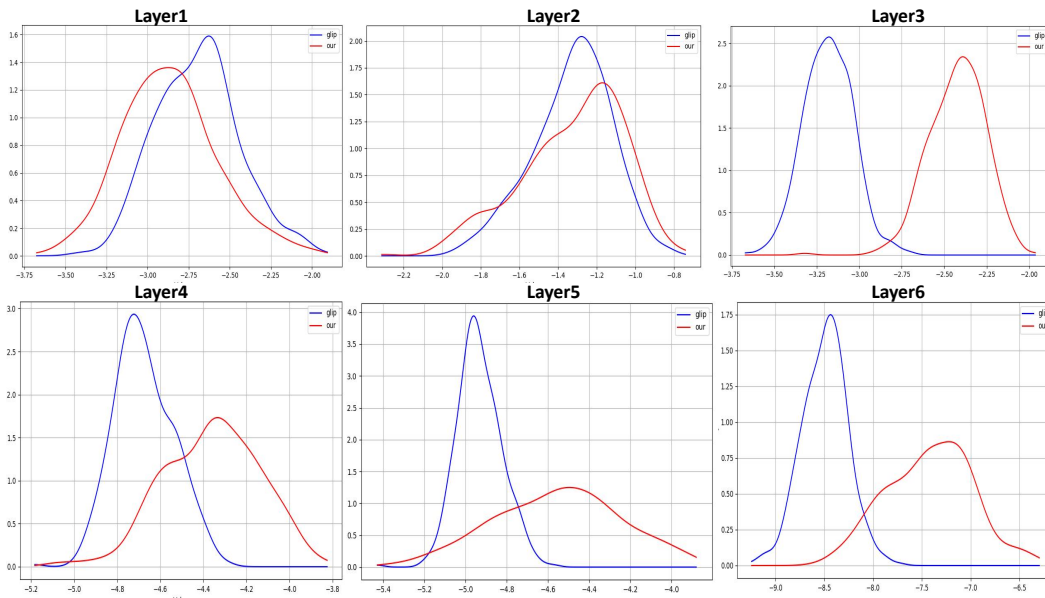


Figure E: Feature distribution of the average attention strength using KDE estimation on five datasets (cvc300, colondb, clinicdb, kvasir etis). The x-axis is the value and the y-axis is the density.

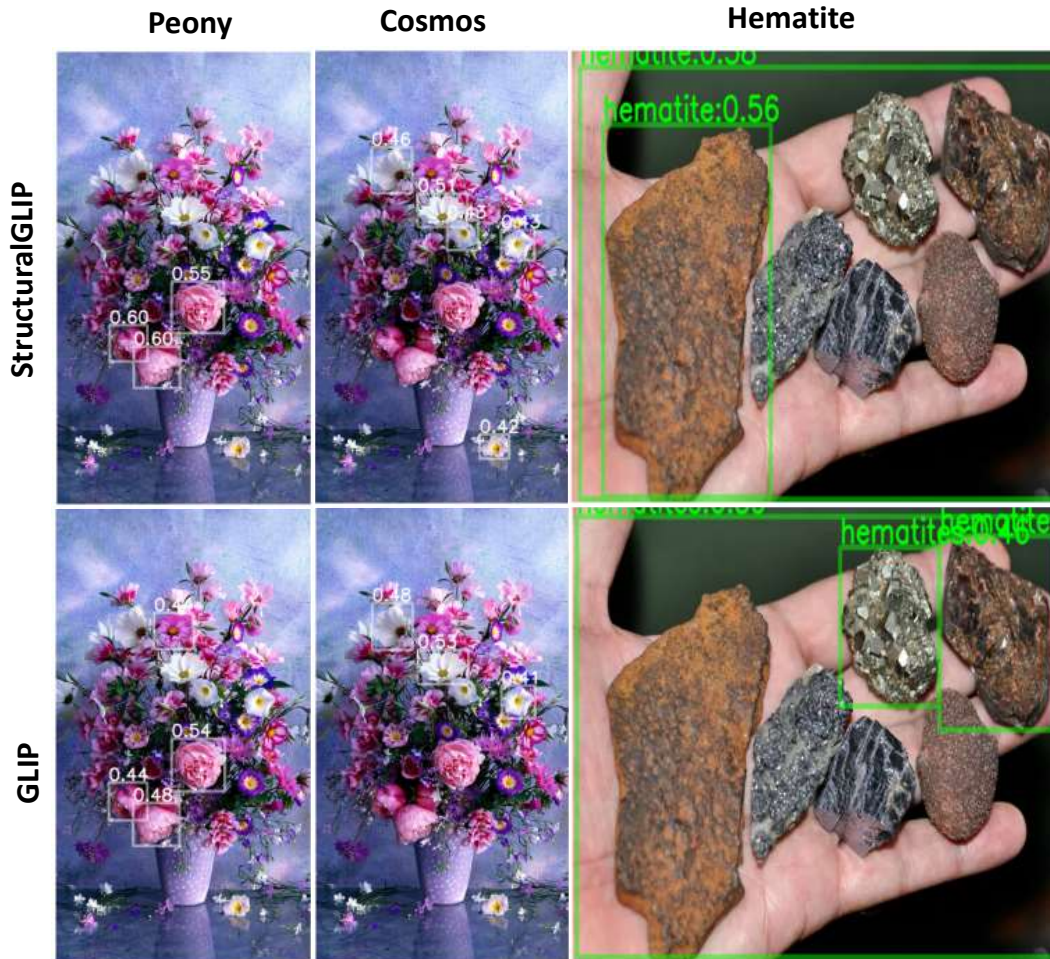


Figure F: Examples of natural images with GLIP and StructuralGLIP.